Quantitative decorating Ni-sites for water-oxidation with the synergy of electronegative sites and high-density spin state

Yayin Li [a,1], Mengwei Yuan [b,1], Han Yang [a,1], Kefan Shi [a], Zemin Sun [b], Huifeng Li [a], Caiyun Nan [a], Genban Sun [a,b,*]

[a] *Beijing Key Laboratory of Energy Conversion and Storage Materials Institution, College of Chemistry, Beijing Normal University, Beijing 100875, China*
[b] *Center for Advanced Materials Research, Beijing Normal University, Zhuhai 519087, China*

ABSTRACT

Oxygen evolution reaction (OER) is the rate-limiting step in water-splitting. The spin-state transition of H_2O/OH^- to O_2 is the critical contributor to slow kinetics, but has not yet received insufficient attention, and model catalysts with explicit active sites are scarce. Herein, we regulated the electronic structure and spin state density of Ni-sites by introducing transition metals into Ni-MOF (NiM-MOF, M = Cr, Mn, Fe, Co, and Cu). Theoretical calculations and experimental results indicated that OER activity has a volcanic relationship with the d-band center, where NiFe-MOF was at the volcano summit, showing an ultra-low overpotential of 172 mV at 10 mA cm^{-2}, which was currently one of the highest catalytic activities. Benefiting from the synergistic effect of electronegativity sites and high-density spin state, balanced the adsorption/desorption of intermediates, and minimized the energy barrier for OER. This work provides a new reference for understanding the catalytic mechanism and designing spin electrocatalysts.

1. Introduction

Oxygen evolution reaction (OER) and hydrogen evolution reaction (HER) are two important half-cell reactions in electrochemical water-splitting, respectively. Compared to HER, OER is a complex process that involves a four-electron and proton transfer associated with O-O formation and O-H cleavage, with sluggish reaction kinetics, which severely limits the energy conversion efficiency of water electrolysis and impedes the industrialization of related devices [1–3]. In principle, the reactant OH^-/H_2O possesses a singlet ground spin state with all paired electrons, while the ground spin state of the product O_2 is a triplet state with two unpaired electrons, and the corresponding Hamiltonian excludes the spin operator, so this transition between different spin states is slow [4–6]. Therefore, to improve the OER conversion efficiency, the controllable regulation of orbital interactions and electron transfer will be crucial. Currently, the theoretical research insights of oxygen electrocatalysis primarily focus on the thermodynamic process of adsorption/desorption between intermediates and active sites [7], while spin-polarized regulation of catalytic activity is still in its infancy.

In actuality, the surface reaction energy barrier and bulk conductivity have a significant impact on the measured overpotential of OER electrocatalysts [8–10]. Although significant progress has been made in improving OER conversion efficiency by modifying the morphological structure [11,12] and composition [13,14] of catalyst nanomaterials, it remains empirical and lacks fundamental theoretical guidance [15]. Investigating the electron spin behavior during interface and bulk transport and optimizing the electronic structure of catalysts is a flexible and direct strategy, which can effectively reduce the reaction overpotential and boost OER catalytic activity. For instance, Sun's group successfully optimized the spin state of Fe^{III} sites through the Jahn-Teller effect of Cu^{2+} to convert NiFe-LDHs from ferrimagnets to ferromagnets, achieving an ultra-low overpotential of 180 mV [16]. Xu et al. designed an interfacial ferromagnetic-antiferromagnetic (FM-AFM) coupling of core-shell samples, which favored the selective removal of electrons with opposite spin directions to the FM core magnetic moment, thereby improving OER kinetics [17]. In addition, Zou et al. exploited the synergistic effect of Fe^{III} and TiO_2 nanobelt to lower the spin state of Fe^{III}, improved electrical conductivity and adsorption with

oxygen-containing intermediates, and boosted the OER catalytic activity [18]. Although optimizing the spin state to improve OER performance is a promising novel approach, the majority of electrocatalysts still have unclear active sites and inhomogeneous compositions. Given this situation, two-dimensional metal-organic frameworks (2D MOFs) with well-defined active centers, uniform morphology, and excellent electron transfer should be selected as model catalysts [19–21]. Ultrathin Ni-MOF nanosheets have been investigated and demonstrated to have excellent OER performance among various 2D MOFs [22,23]. To further clarify the relationship between electronic structure and OER performance, it is critical to use Ni-MOF as the host material and introduce 3d transition metals with different electronegativity to form 2D Ni-based bimetal-organic frameworks to promote the redistribution of spin and charge density.

Inspired by these ideas, we rationally designed the introduction of transition metals (Cr, Mn, Fe, Co, and Cu) with different electronegativity into Ni-MOF, and investigated the relationship between the electronic structure of Ni sites and OER electrocatalytic activity. Density functional theory (DFT) calculations results demonstrated that the electrocatalytic activity of 2D Ni-based bimetallic MOFs had a strong volcanic relationship with the d-band center, which was determined by the introduced electronegativity sites that modulate the electronic structure of the Ni sites. Among these, the introduction of Fe effectively regulated the electronic structure and spin state density with highly active Ni sites, balancing the adsorption/desorption of intermediates, and minimizing the energy barrier for OER, thereby enhancing the intrinsic activity of electrocatalysts. Benefiting from the synergistic effect of electronegativity sites and high-density spin state, NiFe-MOF exhibited an ultralow overpotential of 172 mV at 10 mA cm^{-2}, which was significantly lower than that of other 2D Ni-based MOFs (Ni-MOF and NiM-MOF) and commercial RuO$_2$, and has one of the best OER performances among the current powder electrocatalysts. This work provides new insights into the effects of spin states and electronegativity sites on OER performance at the electronic level, which will aid in the further development of high-performance novel electrocatalysts.

2. Experimental section

2.1. Materials

N, N-dimethylformamide (DMF), FeCl$_3$•6H$_2$O, and CoCl$_2$•6H$_2$O were purchased from Weiss (Beijing) Experimental Supplies Co., Ltd. Anhydrous ethanol (EtOH) and triethylamine (TEA) were obtained from Beijing Chemical Plant. Cr(NO$_3$)$_3$•9H$_2$O and MnCl$_2$•4H$_2$O were purchased from Aladdin Reagent Co., Ltd., Tianjin Komiou Chemical Reagent, and Tianjin damao chemical reagent, respectively. NiCl$_2$•6H$_2$O and CuCl$_2$•2H$_2$O were obtained from Tianjin Bodi Chemical Co., LTD. The distilled water (DIW) was obtained by ion exchange and filtration. All chemicals and solvents were analytical grade and used without further purification in this experiment.

2.2. Synthesis of 2D NiM-MOF (M= Cr, Mn, Fe, Co, and Cu)

In a typical experiment, 32 mL N, N-dimethylformamide (DMF), 2 mL anhydrous ethanol (EtOH), and 2 mL deionized water (DIW) were first mixed to form a homogeneous solution. Subsequently, 0.675 mmol NiCl$_2$•6H$_2$O, 0.075 mmol FeCl$_3$•6H$_2$O (or Cr(NO$_3$)$_3$•9H$_2$O or MnCl$_2$•4H$_2$O or CoCl$_2$•6H$_2$O or CuCl$_2$•2H$_2$O) and 0.75 mmol terephthalic acids were added into the above mixture solution and stirring for 30 min. Then, 0.8 mL triethylamine (TEA) was injected into the above solution. After 8 h of continuous ultrasound at ambient conditions, the samples were first washed three times with DMF and then once with EtOH, and finally vacuum-dried at 60 °C for 12 h to obtain samples labeled as NiFe-MOF, NiCr-MOF, NiMn-MOF, NiCo-MOF, and NiCu-MOF, respectively.

2.3. Synthesis of 2D Ni-MOF

Ni-MOF was prepared by the same method, but only NiCl$_2$•6H$_2$O (0.75 mmol) was added as the metal precursor.

2.4. Materials characterizations

The morphology of the as-prepared materials was observed by field emission scanning electron microscopy (FESEM, Hitachi, SU-8010) with an acceleration voltage of 5 kV. Transmission electron microscopy (TEM) and energy-dispersive X-ray spectroscopy (EDS) elemental mapping were recorded on Talos F200S at 200 kV. High-resolution transmission electron microscopy (HRTEM) measurements were carried out on FEI TF20 working at 80 kV. Atomic force microscopy (AFM) was performed using Nanoscope VIII MultiMode, Bruker with tapping mode. The test of Brunauer-Emmett-Teller (BET) surface area was performed by N$_2$ adsorption-desorption isotherm (SADI) analysis at 77 K using a Quadrasorb SI analyzer. Barrett-Joyner-Halenda (BJH) method was used to calculate pore size distribution. X-ray powder diffraction (XRD) of samples was recorded using a Phillips X′pert ProMPD diffractometer with Cu Kα radiation (λ = 1.54056 Å). Fourier transform infrared (FT-IR) spectra were measured on a Nicolet-380 Fourier-Transform infrared spectrometer using the KBr pellet in the range of 2000–1000 cm^{-1}. X-ray photoelectron spectroscopy (XPS) measurements were performed on an ESCALAB 250Xi spectrometer (Thermo Fishe). Raman spectra were recorded on a microscopic confocal Raman spectrometer (LabRAMAramis, Horiba JobinYivon) with an excitation laser wavelength of 532 nm. The inductively coupled plasma emission spectrometer (ICP-AES, Spectro Arcos) is used for the quantitative determination of metal elements.

2.5. Electrochemical measurements

All catalyst inks were prepared by dispersing 8 mg of the catalyst in the 2 mL of mixed solution (the ratio of ethanol, deionized water and 5% Nafion is 1:0.96:0.04), followed by ultrasonication for 30 min to get a homogeneous suspension. Subsequently, 10 μL of ink was covered on the glassy carbon electrode and dried at room temperature for measurement. The electrochemical performance of all the prepared electrocatalysts was measured in a standard three-electrode system using the electrochemical workstation (CHI 660, Shanghai Chenhua, China). The catalyst-loaded glassy carbon electrode (3 mm diameter), Hg/HgO electrode, and Pt plate were used as the working electrode, reference electrode, and counter electrode, respectively. All the potentials were recorded relative to the reversible hydrogen electrode (RHE) according to the Nernst equation: $E_{RHE} = E_{Hg/HgO} + 0.926$, and the overpotential at 10 mA cm^{-2} (η_{10}) for OER is calculated according to the formula: $\eta_{10} = E_{RHE} - 1.23$ V. OER measurements were carried out in 1.0 M KOH electrolyte. The linear sweep voltammetry (LSV) was performed at the potential range from 0.015 to 1.105 V (vs. Hg/HgO) and a scan rate of 10 mV/s. The electrochemical active surface area (ECSA) of the as-synthesized electrocatalysts was estimated by the double-layer capacitance (C_{dl}), which was measured by the cyclic voltammetry (CV) under the potential window of 0.08–0.18 V (vs. Hg/HgO) with a different scan rate of 10, 20, 40, 60, 80, 100 mV/s. In addition, the long-term stability of the prepared electrocatalysts was recorded by chronoamperometry measurement at 0.6 V (vs. Hg/HgO). The electrochemical impedance spectroscopy (EIS) was carried out at the potential of 5 mV (vs. Hg/HgO), a frequency range of 10 mHz-1000 kHz and the amplitude of a sine wave was 5 mV.

2.6. DFT calculations

Based on the spin-polarized density functional theory (DFT) and the projector-augmented wave method [24] implemented in the Vienna Ab initio Simulation Package (VASP), the density of states was calculated by

the Perdew-Burke-Ernzerhof functional [25,26] within the meta-generalized-gradient approximation [27]. The effective interaction strengths (U_{eff} = U - J) of different 3d orbitals were set as 3.8 = 3.8–0.0 for Ni, 5.0 = 5.0–0.0 for Cr, 4.0 = 5.0–1.0 for Mn, 4.0 = 5.0–1.0 for Fe, 4.0 = 4.0–0.0 for Co, and 5.0 = 5.0–0.0 for Cu atoms [28–31]. A plane-wave basis set [32] was used with a kinetic energy cutoff of 520 eV with a K-point grid of $2 \times 2 \times 2$, using the Gamma-centered method. A vacuum layer of 10 Å was applied to decouple adjacent atomic slabs. The convergence criterion for force was 0.01 eV Å^{-1}. The $E_{adsorpation}$ was described with the formula [33].
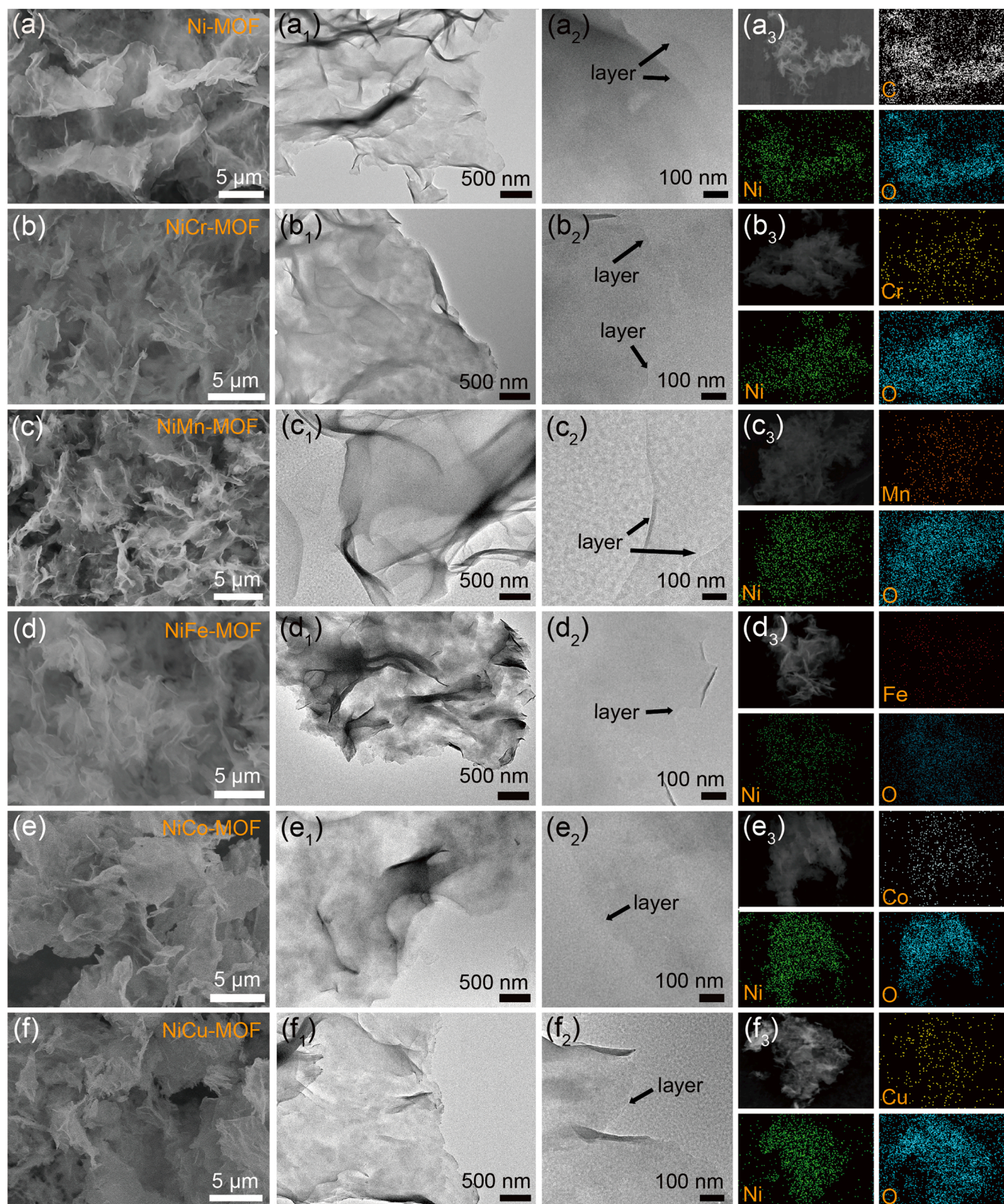
Fig. 1. (a-f) SEM images, (a_1-f_1 and a_2-f_2) TEM images, and (a_3-f_3) elemental mapping images of Ni-MOF and NiM-MOF (M= Cr, Mn, Fe, Co, and Cu).

$$E_{adsorption} = -\,(E_{sample/intermediate} - E_{sample} - E_{intermediate})$$

where $E_{sample/intermediate}$, E_{sample}, and $E_{intermediate}$ were the total energy of the electrocatalyst plus intermediate, the energy of the isolated electrocatalyst surface, and the energy of the free intermediate.

3. Results and discussion

3.1. Structural characterization of Ni-based MOFs

The scanning electron microscopy (SEM) and transmission electron microscopy (TEM) were first performed to investigate the morphology and structure of the synthesized Ni-based MOFs. It can be observed that Ni-MOF and all bimetallic MOFs have ultrathin 2D nanosheet morphology with transverse dimensions ranging from hundreds of nanometers to several micrometers, and the flexible nanosheets at the edges also curl spontaneously upon drying, as shown in Fig. 1. This indicates that the morphologies of the nanosheets are well maintained when Cr, Mn, Fe, Co, and Cu are doped into Ni-MOF and have high specific surface areas, which facilitates the full exposure of the active sites. Furthermore, the Ni, M (M = Cr, Mn, Fe, Co, and Cu) and O elements of the bimetallic MOFs are found uniformly distributed on the ultrathin nanosheets compared to the elemental mapping of the monometallic Ni-MOF (Fig. 1a₃-f₃), effectively demonstrating the successful doping of the transition metals Cr, Mn, Fe, Co, and Cu, respectively.

The bimetallic NiFe-MOF was thoroughly explored to learn more about the catalyst structure. The high-resolution transmission electron microscopy (HRTEM) in Fig. 2a-b reveals that the lattice fringes spacings of Ni-MOF and NiFe-MOF are 1.02 nm and 1.03 nm, respectively, both corresponding to the (200) crystal plane, suggesting that the (200) plane of the synthesized catalysts is the most exposed to the solution during OER process [34]. Meanwhile, the clear lattice texture indicates that the
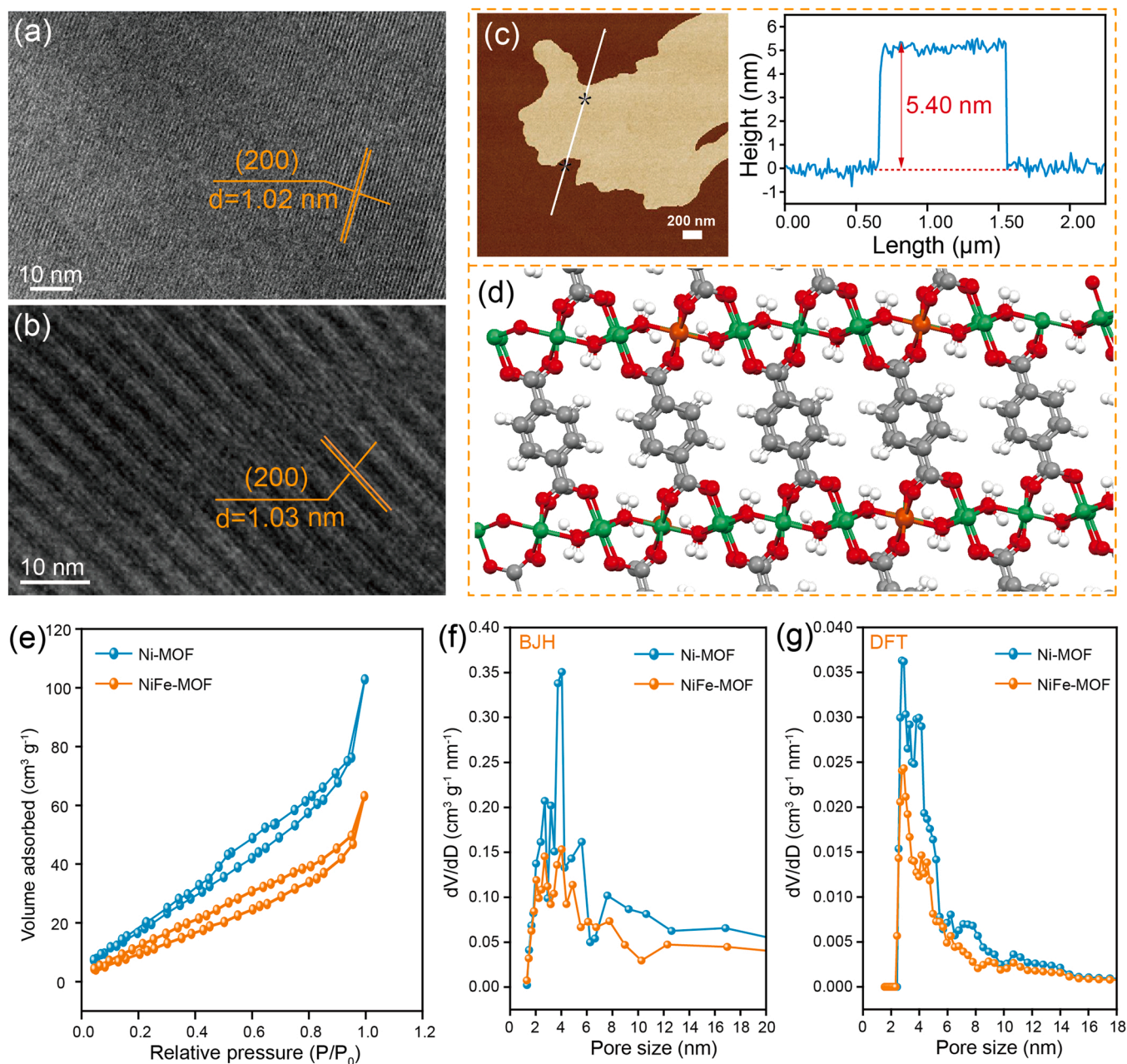

Fig. 2. HRTEM images of (a) Ni-MOF and (b) NiFe-MOF nanosheets. (c) The AFM image and height variation curves along the marking line direction for NiFe-MOF. (d) Theoretical structure model image of NiFe-MOF. (e) N₂ adsorption-desorption isotherms and (f-g) pore size distributions for Ni-MOF and NiFe-MOF.

sample has high crystallinity and strong stability. The analysis of surface activity effect by sample thickness is crucial. Atomic force microscopy (AFM) images (Fig. S1 and Fig. 2c) show that the surfaces of Ni-MOF and NiFe-MOF 2D nanosheets are relatively flat, where NiFe-MOF nanosheets are thicker than Ni-MOF with a thickness of 5.4 nm, corresponding to seven metal coordination layers [35], the overall structure is periodically arranged (Fig. 2d). This result indicates that the introduction of the second metal will increase the thickness of the nanosheets and decrease the specific surface area. The pore structure and specific surface area of the materials were analyzed by N_2 adsorption-desorption isotherm. As shown in Fig. 2e, Ni-MOF and NiFe-MOF could be recognized as a type II isotherm with H3-type hysteresis loops, which may be ascribed to the aggregation of nanosheets forming slit-like mesopores, with pore sizes ranging from 2 to 10 nm (Fig. 2f-g), have crystallographic nature with close packing (absence of microporous adsorption) [36]. The Brunauer-Emmett-Teller (BET) specific surface area of 101.8 m^2 g^{-1} for NiFe-MOF is slightly lower than that of Ni-MOF (149.0 m^2 g^{-1}), which is consistent with AFM results, demonstrating that catalytic activity is not primarily influenced by surface area.

Fig. 3a displays that all 2D Ni-based MOFs have similar X-ray powder

diffraction (XRD) patterns and a comparative match with the simulated crystal structure (CCDC No. 985792), all with characteristic diffraction peaks between 8° and 10°, which can be ascribed to the (200) crystal plane [23]. A closer examination reveals that the diffraction peaks corresponding to the (200) crystal plane of the bimetallic MOFs are all shifted to smaller angles, indicating that second metals (Cr, Mn, Fe, Co, and Cu) are successfully inserted into the Ni-MOF, respectively, which can be distinctly observed from the enlarged XRD pattern in Fig. 3b. The inductively coupled plasma emission spectrometer (ICP-AES) measurements showed that the proportion of hetero elements in the bimetallic structure was ca. 9/1, and close to the feed ratio during the experiment (Table S1). The Fourier transform infrared spectroscopy (FT-IR) was performed to further comprehend the structural information of Ni-based MOFs. As shown in Fig. S2, all bimetallic MOFs demonstrate similar FT-IR spectra to that of Ni-MOF. The peaks locate at 1320 and 1690 cm^{-1} are attributed to the characteristic absorption of O=C-O, the bending vibration absorption peak of C=O locate at 1380 cm^{-1}, and the absorption band is caused by the symmetric stretching of C=C in the benzene skeleton locate at 1500 and 1580 cm^{-1} [28]. The presence of these specific functional groups indicates that formed MOFs contained
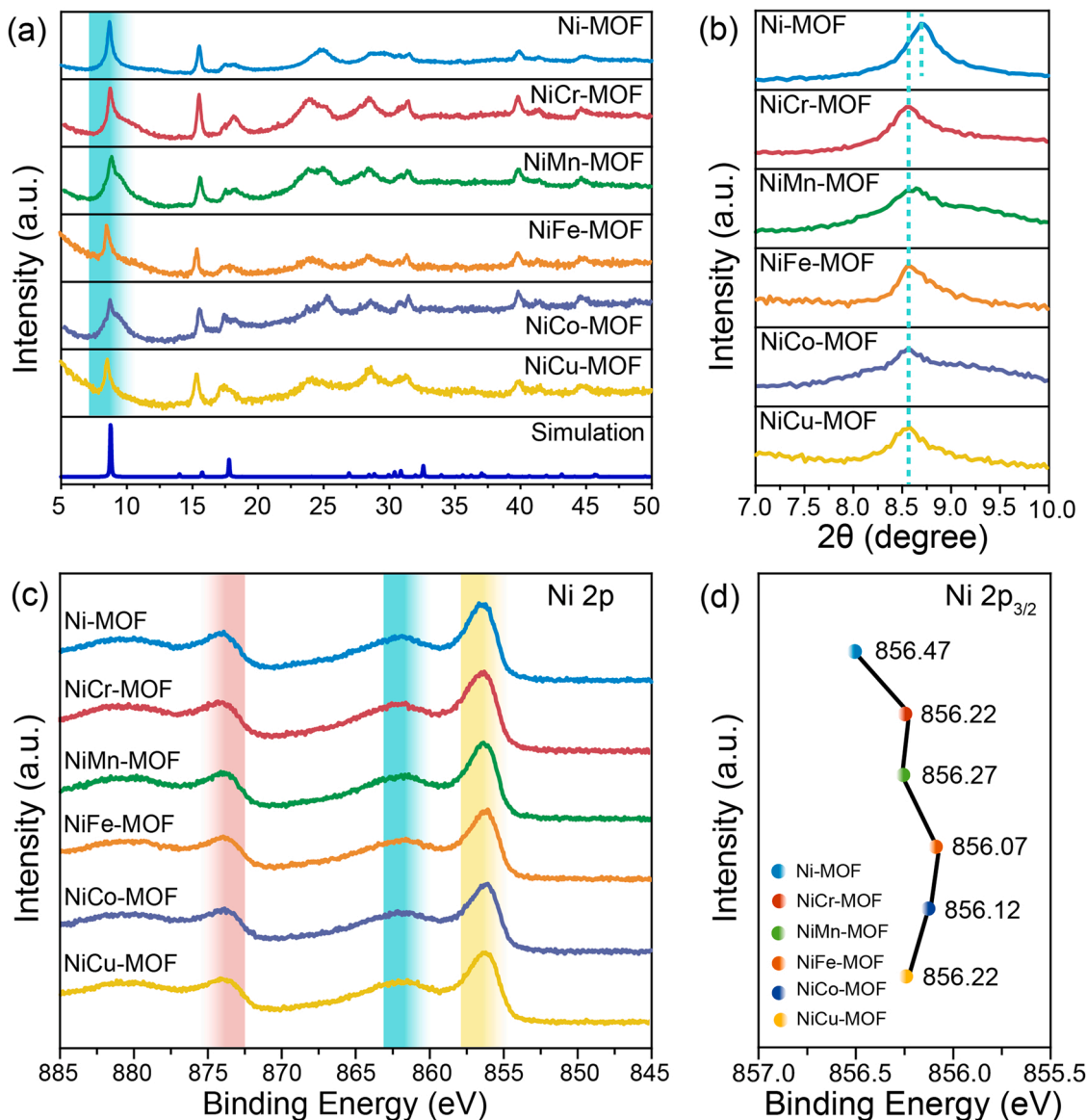
Fig. 3. (a) XRD patterns, and (b) the corresponding enlarged XRD patterns of 2D Ni-based MOFs. (c) Ni 2p XPS spectra, and (d) the corresponding Ni 2p$_{3/2}$ binding energy values of 2D Ni-based MOFs.

the benzene ring, C-O, and C=O, which are consistent with the functional groups contained in the ligand terephthalic acid, further confirming that the as-synthesized 2D Ni-based MOFs are organic framework materials formed by coordination with metal ions and the terephthalic acid ligands.

To explore the chemical valence and surface composition, X-ray photoelectron spectroscopy (XPS) analysis was performed. Fig. S3 shows the binding energy plots of 2D NiM-MOF (M= Cr, Mn, Fe, Co, and Cu). The Cr 2p XPS spectrum of NiCr-MOF (Fig. S3a) exhibits two peaks at approximately 577.87 (Cr $2p_{3/2}$) and 587.67 eV (Cr $2p_{1/2}$), which can be attributed to Cr^{3+} [37]. The Mn 2p XPS spectrum of NiMn-MOF (Fig. S3b) could be fitted into two characteristic peaks at 642.42 and 653.32 eV, which are well ascribed to the Mn $2p_{3/2}$ and Mn $2p_{1/2}$, respectively, indicating the oxidation state of Mn is + 2 [38]. The characteristic peaks of NiFe-MOF at 713.57 and 724.57 eV (Fig. S3c) are identified as Fe^{3+} species, which corresponded to Fe $2p_{3/2}$ and Fe $2p_{1/2}$ binding energies, respectively [39]. As shown in Fig. S3d, the Co 2p XPS spectrum of NiCo-MOF could be divided into two peaks at the binding energy of 781.67 and 797.32 eV, corresponding to Co $2p_{3/2}$ and Co $2p_{1/2}$, respectively, suggesting the existence of Co^{2+} [40]. In addition, the Cu 2p XPS spectrum of NiCu-MOF (Fig. S3e) displays a pair of spin-orbit doublets peaks of Cu^{2+} at 934.37 and 953.62 eV, which belongs to Cu $2p_{3/2}$ and Cu $2p_{1/2}$, respectively [41]. The above results

show that the valence states of all metal ions do not change before and after the reaction.

We further investigated the electronic interaction of Ni-based MOFs and analyzed the valence state of the main metallic element Ni in the samples. In the Ni 2p XPS spectrum of Ni-MOF (Fig. 3c), the spin-orbit doublets of Ni $2p_{3/2}$ and Ni $2p_{1/2}$ are located at 856.47 and 873.92 eV, respectively [42], indicating the existence of Ni^{2+}. After the introduction of different metals, the orbital binding energy of Ni $2p_{3/2}$ changes to varying degrees (Fig. 3d), indicating that the introduction of other metals has a modulating effect on the electronic structure of the Ni sites, which may be primarily due to differences in electronegativity [43, 44]. Among all the bimetallic MOFs, NiFe-MOF has the most pronounced negative shift with a Ni $2p_{3/2}$ of 856.07 eV, showing that the introduction of Fe can effectively regulate the electronic structure of the Ni sites.

3.2. Evaluation of OER performance

The OER performance evaluation of the as-synthesized 2D Ni-based MOFs using a standard three-electrode system in 1.0 M KOH electrolyte, and commercial RuO_2 was also measured under the same conditions. According to the linear sweep voltammetry (LSV) curves (Fig. 4a), a typical anodic peak can be captured at 1.25–1.4 V (vs. RHE) of OER
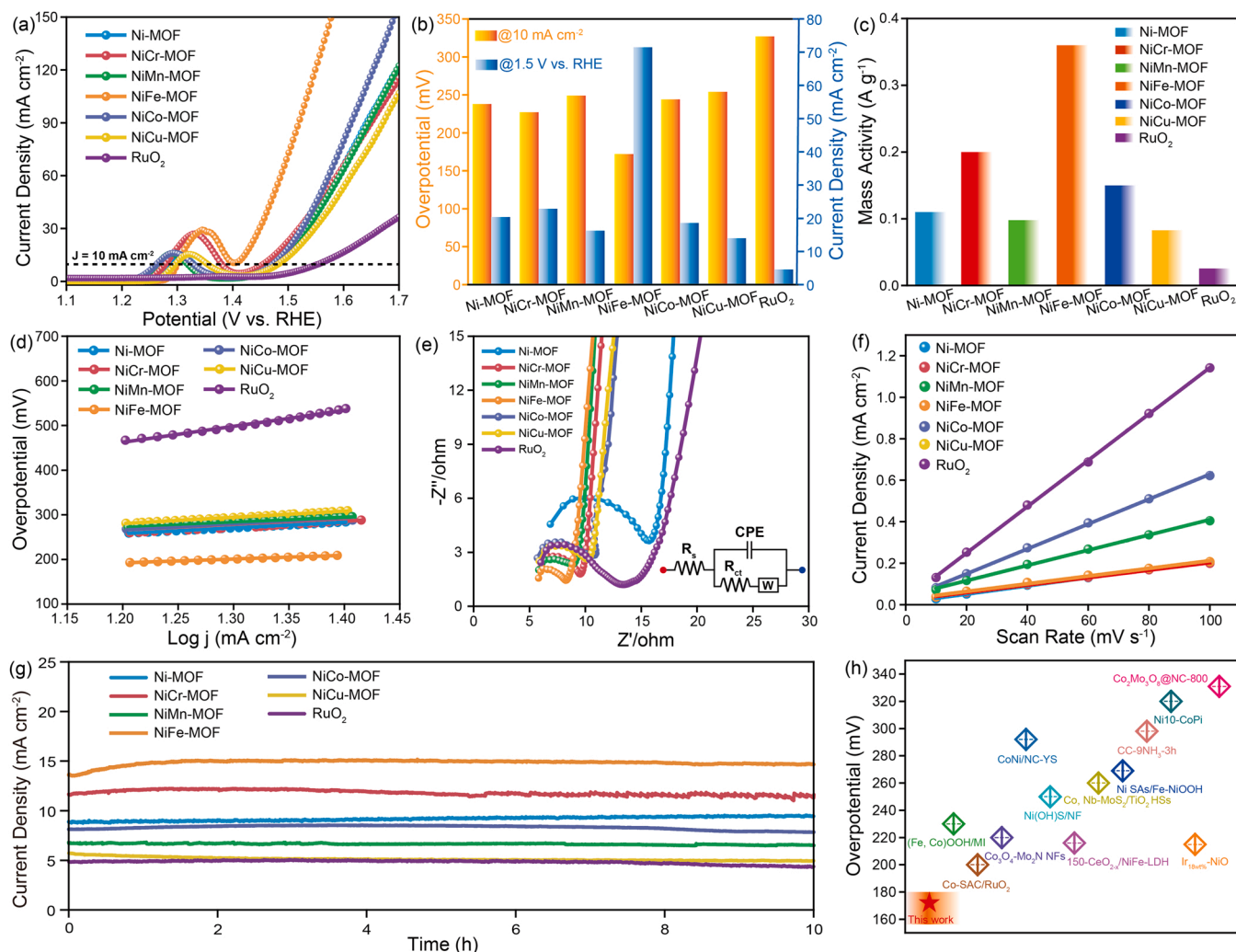
Fig. 4. OER performance of 2D Ni-based MOFs and RuO_2 at 1.0 M KOH: (a) OER polarization curves, (b) histograms of the overpotential at 10 mA cm^{-2} and current density at 1.5 V (vs. RHE), (c) mass activity, (d) Tafel plots, (e) Nyquist plots (the inset is an equivalent circuit), (f) plots of current density vs. scan rate at 1.05 V (vs. RHE), and (g) I-T curves. (h) Comparison of the OER performance of the NiFe-MOF electrocatalysts in this work with some other recently reported high-performance electrocatalysts in 1.0 M KOH.

polarization curves for Ni-based MOFs, which can be attributed to the oxidation of Ni^{2+} to Ni^{3+}, and visibly observation is that NiFe-MOF has the highest peak and the most positive shift, frequently occurs in Fe modified Ni-based OER electrocatalysts [45]. However, in order to acquire the true catalytic activity of the samples, we avoided the oxidation peak region, and ultimately obtained the order of activity of the electrocatalysts is NiFe-MOF > NiCr-MOF > Ni-MOF > NiCo-MOF > NiMn-MOF > NiCu-MOF > RuO_2. Fig. 4b provides more specific information, NiFe-MOF exhibits an ultra-low overpotential of 172 mV and a maximum current density of 73.00 mA cm^{-2} at 10 mA cm^{-2} and 1.5 V (vs. RHE), respectively, which is much better than NiCr-MOF (227 mV, 22.69 mA cm^{-2}), Ni-MOF (237 mV, 20.18 mA cm^{-2}), NiCo-MOF (244 mV, 18.58 mA cm^{-2}), NiMn-MOF (249 mV, 16.24 mA cm^{-2}), NiCu-MOF (254 mV, 13.99 mA cm^{-2}), and RuO_2 (327 mV, 4.59 mA cm^{-2}). In addition, the mass activity of Ni-based MOFs was calculated, and the results are shown in Fig. 4c, where Fe has the highest mass activity, which is 3.3-fold that of Ni-MOF and 10-fold that of commercial RuO_2. The above results show that the OER performance of Ni-based MOFs is completely superior to that of commercial RuO_2, proving our universality, and NiFe-MOF has the most outstanding performance, demonstrating that the introduction of Fe can most effectively improve the catalytic activity. The OER kinetics of the electrocatalysts is investigated as shown in Fig. 4d and Fig. S4. As expected, NiFe-MOF exhibits the lowest Tafel slope of 85.53 mV dec^{-1}, which is smaller than those of Ni-MOF (127.92 mV dec^{-1}), NiCr-MOF (136.37 mV dec^{-1}), NiMn-MOF (117.99 mV dec^{-1}), NiCo-MOF (105.24 mV dec^{-1}) and NiCu-MOF (138.50 mV dec^{-1}), and significantly lower than RuO_2 (356.44 mV dec^{-1}), possess the fastest reaction kinetics of OER. This implies that Fe can raise electron mobility by optimizing the electron spin state. To investigate the electrode reaction kinetics and elucidate the origin of the high OER activity of NiFe-MOF, electrochemical impedance spectroscopy (EIS) measurements of different samples were carried out under the identical conditions. The charge transfer resistance (R_{ct}) was derived by fitting a Nyquist plot of the EIS spectrum (Fig. 4e) through an equivalent circuit model (Inset in Fig. 4e). As shown in Fig. S5, the R_{ct} of the bimetallic MOFs were all significantly lower than that of the Ni-MOF and commercial RuO_2, in particular, NiFe-MOF exhibits the lowest charge transfer resistance ($R_{ct} = 5.304\ \Omega$), indicating that the introduction of electronegative sites (Cr, Mn, Fe, Co, Cu) could facilitate the charge transfer in Ni-MOF, and the Fe electronegativity sites contribute most to the charge transfer at the electrolyte-catalyst interface, consistent with its highest OER activity, which may be ascribed to the Fe electronegativity sites play the greatest role in optimizing the electron spin structure of the Ni sites. In addition, we calculated the electrochemical double-layer capacitance (C_{dl}) through the cyclic voltammetry (CV) test in the non-Faradaic region, and evaluated the electrochemical active surface area (ECSA). According to Fig. S6 and Fig. 4 f, the C_{dl} values of Ni-MOF, NiCr-MOF, NiMn-MOF, NiFe-MOF, NiCo-MOF, NiCu-MOF, and RuO_2 are 1.98 mF cm^{-2}, 1.81 mF cm^{-2}, 3.86 mF cm^{-2}, 1.86 mF cm^{-2}, 6 mF cm^{-2}, 1.86 mF cm^{-2}, and 11.17 mF cm^{-2}, respectively. Apparently, the great mass of Ni-based MOFs have a larger active area compared to NiFe-MOF, but this result is inconsistent with the catalytic activity. This may be attributed to the fact that some of the electrochemical active sites do not possess catalytic activity [46], or the utilization of portion active sites is limited [47], so the difference in catalyst performance cannot depend entirely on the electrochemical active surface area. This also indicates that the high activity of NiFe-MOF may stem from the fast mass/charge transfer caused by Fe electronegativity sites, and the fast kinetic reaction induced by the active site in effective contact with the electrolyte. Long-term stability is a crucial criterion to evaluate whether electrocatalysts have practical application value. As shown in Fig. 4 g, the current density of the sample is consistent with the overpotential result, confirming that the catalytic activity of Ni-based MOFs is higher than that of RuO_2. And after 10 h of electrolysis, the current density has almost no or little attenuation, exhibiting good durability. According to

the XPS results after stability testing (Fig. S7), we find that the Ni 2p spectra of Ni-based MOFs have a significant peak at Ni $2p_{3/2}$ (858.9 eV), which is mainly related to the binding energy of the NiOOH structure [48,49], indicating that the formed NiOOH is the active site for OER. Furthermore, we compared the most outstanding NiFe-MOF to the OER electrocatalysts reported in recent years and discovered that NiFe-MOF is on par with or even superior to the state-of-the-art (Fig. 4 h) [50–61].

3.3. Analysis of the electronic structure and spin state for Ni sites

Electron structure is an important factor in determining the performance of the materials in electrocatalysis. The accurate and fine electronic structure research and descriptors are of great significance to deeply understand the structure-activity relationship of materials. Thence, we constructed Ni-MOF model catalysts with a $2 \times 2 \times 1$ supercell, and after considering the atomic proportion and the equivalence of Ni atoms in Ni-MOF, we chose to replace one of the Ni atoms (Ni_{12}) with other metal atoms M (M = Cr, Mn, Fe, Co, and Cu) to form a Ni_xM_{1-x}-MOF (x ≈ 0.9) bimetallic structure with 9/1 metal atoms ratio (Fig. S8), thus taking advantage of the change in the d-band center of Ni to describe the relationship between material properties and electronic structure. Fig. 5a and Fig. S9 present the optimized structure of the prepared 2D Ni-based MOFs. All these supercells demonstrated the same crystal structure with no change. In particular, the values of electron local function towards different Ni-based MOFs are close, indicating no change in the properties of the chemical bonds (Fig. 5b, Fig. S10 and Table S2). These results provide the conditions of relative equality. As shown in Fig. S11, the total density of states (TDOS) and the partial density of states (PDOS) present that most of the Ni-based MOFs (Ni-MOF, NiCr-MOF, NiFe-MOF, NiCo-MOF, and NiCu-MOF) have obvious band gaps with semiconductor properties. However, NiMn-MOF exhibits a large variation, which tends to a metallicity with a reduced bandgap, and is accompanied by more active electrons at the Fermi level. This obvious change may result from the difference in the electro-negativity in Ni (1.91) and Mn (1.55). As for the other Ni-based MOFs, the electronegativity between the two metals is close, so presents a minor difference (Table S3). As for the PDOS in Fig. S11f, it also demonstrated the difference between the electron structure and it had an important on the DOS of the MOF matrix. However, the OER performance of NiMn-MOF with more active electrons was not the best, which indicated that there have some other factors to determine the performance. Thus, the more refined changes of single Ni sites may be more able to reflect the role of spin state regulation. The PDOS of different Ni sites (Ni_2, Ni_4, Ni_6, Ni_8) is also considered (Fig. S12-13), with the changed electron structures, which may be acted as the potential high active sites for OER. To further investigate the origin factors, we calculated the d-band center of the Ni sites in Ni-based MOFs. The d-band center of Ni-MOF is − 2.52, and the d-band center changed differently when a second different metal was introduced. The average d-band center value of NiMn-MOF presents a maximum change of − 3.17, and other Ni-based MOFs are − 2.81 (NiCr-MOF), − 2.59 (NiFe-MOF), − 2.78 (NiCo-MOF) and − 2.50 (NiCu-MOF), respectively (Table S4). In the different Ni sites (Ni_2, Ni_4, Ni_6, Ni_8) of bimetal MOFs, the d-band center value also changes consistent with the average value, affected by the introduction of different electronegative sites (Table S5). Fig. 5c-d presents a highly strong volcano relationship between the d-band center and electrocatalytic activity, with the NiFe-MOF located at the volcano summit, implying that the introduction of Fe can effectively optimize the electronic structure and d-band center of Ni sites. And further, we selected the three typical structures of Ni-MOF, NiFe-MOF, and NiCu-MOF as the slabs to adsorb the -OH to evaluate and identify the performance of electrocatalysts. As can be seen from Fig. 5e-f and Fig. S14, NiFe-MOF and Ni-MOF show stronger adsorption energies (E_{ads}) of − 1.98 eV and − 2.65 eV than that of NiCu-MOF (2.00 eV), respectively, which can markedly improve the reaction kinetics and facilitate the OER process. The rate-determining step of OER on the conventional interface or reaction to itself goes
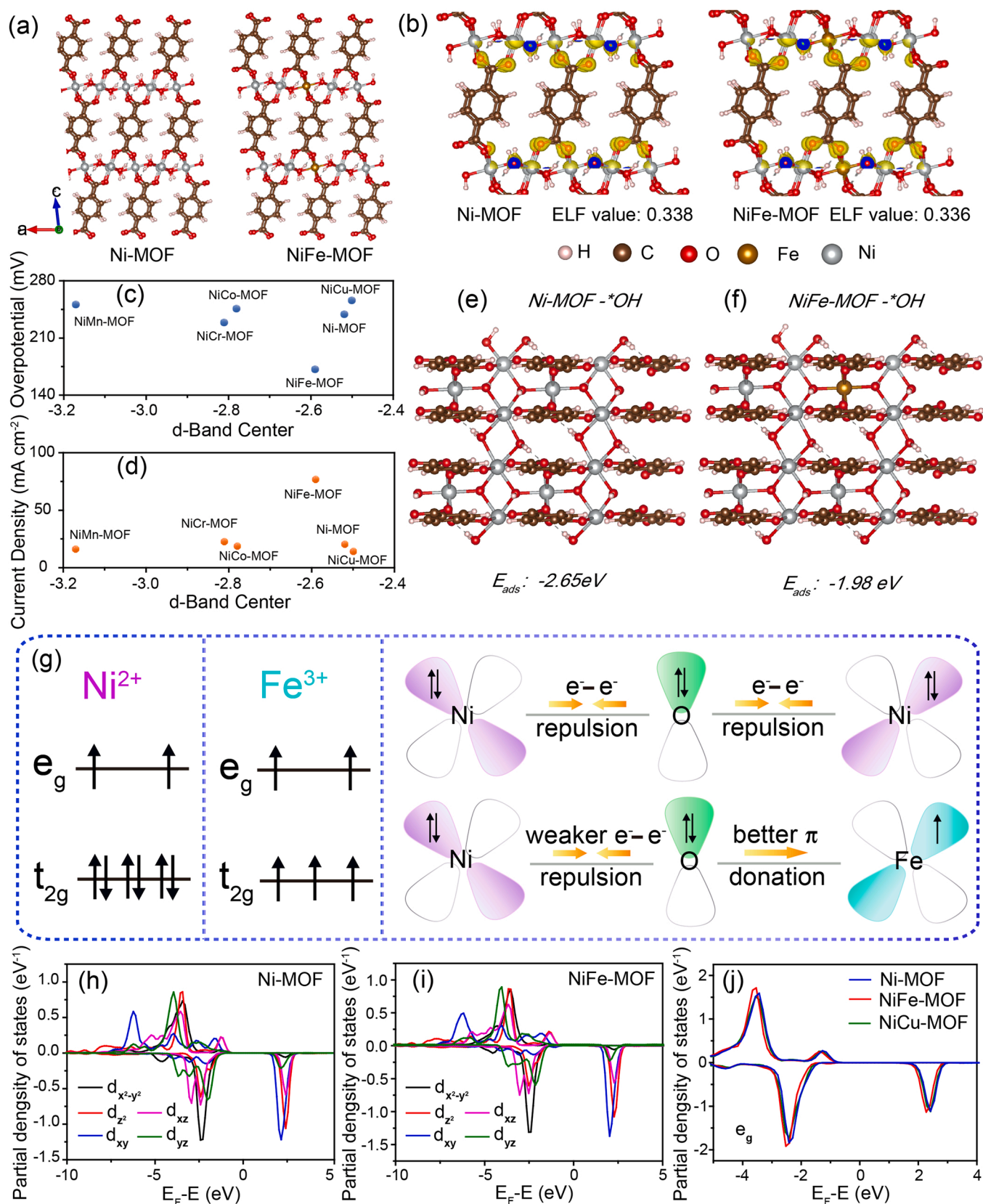
Fig. 5. (a) The optimized structures of the Ni-MOF and NiFe-MOF. (b) The isosurface of the Ni-MOF and NiFe-MOF. The correlation of the (c) overpotential /(d) current density and the d-band center. The adsorption structure towards *OH on (e) Ni-MOF and (f) NiFe-MOF slabs. (g) Schematic representation of the electronic coupling in Ni-MOF and NiFe-MOF. PDOS of the d orbitals for (h) Ni-MOF and (i) NiFe-MOF. (j) PDOS of 3d e_g states in Ni-MOF, NiFe-MOF, and NiCu-MOF.

through the third step of OOH* -O$_2$ [16]. According to the report [62–65], on the interface with NiOOH as the active site, the decisive step is mainly the second step, namely the transition from OH* to O* . For Ni-based OER catalyst materials, especially the Ni-MOFs (BDC) [62], their active sites are mainly NiOOH obtained by electro-oxidation in the reaction process, and with a rate-determining step of OH* -O* . Considering this consequence, we mainly use the adsorption energy and the free energy change to better describe the capture ability of the electrocatalyst to the substrate and whether there is a potential enhancement of the step of OH* to O* to promote the formation of NiOOH in the electro-oxidation process. For the slab that is favorable for adsorption, the appropriate adsorption energy not only has a strong capture capacity for the substrate OH$^-$, but also does not affect the conversion of products in the multi-electron step to the next reaction step OH* -O* , which may be conducive to promoting the reaction. In addition, the formation of O* may promote the conversion of the electrocatalyst itself from the Ni site to NiOOH, and has an important role in accelerating the formation of active sites. Furthermore, the free energy transitions between *OH slab and *O slab for Ni-MOF, NiFe-MOF, and NiCu-MOF are 3.10, 2.62, and 4.31 eV, respectively (Fig. S15-17). NiFe-MOF has the lowest value of free energy differences, and the energy barrier is minimal, resulting in the fastest transformation process. This suggests that the more feasible process occurs on NiFe-MOF slab with a balance in the adsorption and desorption capability towards the oxygen-containing intermediates, with great potential to promote the OER process attaching to the higher electrocatalytic activity.

To further explain the high catalytic activity of NiFe-MOF, we considered the spin states of Fe, Ni, and Cu ions. In the NiFe-MOF, the valence electronic configuration of Fe^{3+} is 3d^5 with the high spin state of unpaired electrons in the π-symmetry (t$_{2g}$) d-orbitals, which interacts with the bridging O^{2-} via π-donation (Fig. 5g) [18]. As a comparison, the π-symmetry (t$_{2g}$) d-orbitals of Ni^{2+} and Cu^{2+}are fully occupied, and thus the major interaction with the bridging O^{2-} is e$^-$-e$^-$ repulsion (Fig. 5g, Fig. S18). When Fe^{3+} is coupled with Ni^{2+}, the π-donation via Fe-O can be strengthened by the electron-electron repulsion between O^{2-} and Ni^{2+} with an obvious changed t$_{2g}$ orbitals, and maybe resulting in the optimization of the intermediate adsorption on Ni sites [16,35], which is not found after the coupling between Cu^{2+} and Ni^{2+} (Fig. 5h-i, Fig. S19). Similarly, the PDOS (Ni$_2$ sites) of the unfilled metal 3d e$_g$-orbitals both in Ni-MOF, NiFe-MOF, and NiCu-MOF suggest that the occupied e$_g$ state in NiFe-MOF tends to lower energy, enabling a high-density spin state (Fig. 5j), which may be more feasibility for the adsorption and desorption of the intermediate in the OER process, with a balance between the adsorption and desorption capability. It has been reported that such coupling could induce a change of e$_g$ filling and further optimize their OER performance [66]. The theoretical and experimental results demonstrate that the modulation of catalytic activity by electronegative sites and spin state density in MOF structures is a reliable method, and provides a novel insight for the design of other high-performance electrocatalysts.

4. Conclusions

In summary, we believe that the introduction of electronegative sites to optimize the electronic structure and spin state density of Ni sites is crucial for boosting OER catalytic activity. DFT calculations and experimental tests revealed that the OER performance of 2D Ni-based MOFs (NiM-MOF, M= Cr, Mn, Fe, Co, and Cu) with well-defined active sites and structure had a significant volcanic relationship with the d-band center, in which NiFe-MOF was at the volcano summit, exhibited an ultra-low overpotential of 172 mV at 10 mA cm^{-2}, which was significantly lower than that of commercial RuO$_2$ by 155 mV, with fast reaction kinetics. The reason was that the addition of Fe can efficiently optimize the electronic structure and spin state density with highly active Ni sites, balanced the adsorption/desorption of intermediates, lowered the energy barrier for electron transfer, and

facilitated the spin transformation of singlet reactants (OH$^-$/H$_2$O) to triplet products (O$_2$), resulting in significantly improved OER performance. Our work provides a new avenue for the design of spin electrocatalysts and further fills the gap in the field of spin behavior in electrocatalysis.

CRediT authorship contribution statement

Genban Sun: Conceived and directed this work. **Yayin Li:** Performed the experiments and data analysis, and wrote the manuscript. **Mengwei Yuan:** Performed the DFT calculations, wrote mechanism analysis, and revised the manuscript. **Han Yang:** Performed the experiments and data analysis. **Kefan Shi:** Helped with electrochemical measurements. **Zemin Sun, Huifeng Li, and Caiyun Nan:** Helped with the data analysis and the writing. All authors discussed the results and provided comments on the manuscript.

Declaration of Competing Interest

The authors declare that they have no known competing financial interests or personal relationships that could have appeared to influence the work reported in this paper.

Data Availability

We choose not to share research data.

Appendix A. Supporting information

Supplementary data associated with this article can be found in the online version at doi:10.1016/j.apcatb.2022.122167.

References

[1] R.Q. Yao, H. Shi, W.B. Wan, Z. Wen, X.Y. Lang, Q. Jiang, Flexible Co-Mo-N/Au electrodes with a hierarchical nanoporous architecture as highly efficient electrocatalysts for oxygen evolution reaction, Adv. Mater. 32 (2020), e1907214, https://doi.org/10.1002/adma.201907214.

[2] X.L. Wang, L.Z. Dong, M. Qiao, Y.J. Tang, J. Liu, Y. Li, S.L. Li, J.X. Su, Y.Q. Lan, Exploring the performance improvement of the oxygen evolution reaction in a stable bimetal-organic framework system, Angew. Chem. Int. Ed. 57 (2018) 9660–9664, https://doi.org/10.1002/anie.201803587.

[3] P. Wang, M. Yan, J. Meng, G. Jiang, L. Qu, X. Pan, J.Z. Liu, L. Mai, Oxygen evolution reaction dynamics monitored by an individual nanosheet-based electronic circuit, Nat. Commun. 8 (2017) 645, https://doi.org/10.1038/s41467-017-00778-z.

[4] O. Mabayoje, A. Shoola, B.R. Wygant, C.B. Mullins, The role of anions in metal chalcogenide oxygen evolution catalysis: electrodeposited thin films of nickel sulfide as "pre-catalysts", ACS Energy Lett. 1 (2016) 195–201, https://doi.org/10.1021/acsenergylett.6b00084.

[5] W. Mtangi, V. Kiran, C. Fontanesi, R. Naaman, Role of the electron spin polarization in water splitting, J. Phys. Chem. Lett. 6 (2015) 4916–4922, https://doi.org/10.1021/acs.jpclett.5b02419.

[6] X. Li, Z. Cheng, X. Wang, Understanding the mechanism of the oxygen evolution reaction with consideration of spin, Electrochem. Energ. Rev. 4 (2020) 136–145, https://doi.org/10.1007/s41918-020-00084-1.

[7] G. Zhou, P. Wang, H. Li, B. Hu, Y. Sun, R. Huang, L. Liu, Spin-sate reconfiguration induced by alternating magnetic field for efficient oxygen evolution reaction, Nat. Commun. 12 (2021) 4827, https://doi.org/10.1038/s41467-021-25095-4.

[8] E.M. Miner, T. Fukushima, D. Sheberla, L. Sun, Y. Surendranath, M. Dinca, Electrochemical oxygen reduction catalysed by Ni$_3$(hexaiminotriphenylene)$_2$, Nat. Commun. 7 (2016) 10942, https://doi.org/10.1038/ncomms10942.

[9] Z. Xue, K. Liu, Q. Liu, Y. Li, M. Li, C.Y. Su, N. Ogiwara, H. Kobayashi, H. Kitagawa, M. Liu, G. Li, Missing-linker metal-organic frameworks for oxygen evolution reaction, Nat. Commun. 10 (2019) 5048, https://doi.org/10.1038/s41467-019-13051-2.

[10] C. Wang, H. Yang, Y. Zhang, Q. Wang, NiFe alloy nanoparticles with hcp crystal structure stimulate superior oxygen evolution reaction electrocatalytic activity, Angew. Chem. Int. Ed. 58 (2019) 6099–6103, https://doi.org/10.1002/anie.201902446.

[11] H. Chu, D. Zhang, B. Jin, M. Yang, Impact of morphology on the oxygen evolution reaction of 3D hollow cobalt-molybdenum nitride, Appl. Catal. B 255 (2019), 117744, https://doi.org/10.1016/j.apcatb.2019.117744.

[12] X. Yang, J. Chen, Y. Chen, P. Feng, H. Lai, J. Li, X. Luo, Novel Co_3O_4 nanoparticles/nitrogen-doped carbon composites with extraordinary catalytic activity for oxygen evolution reaction (OER, Nanomicro Lett. 10 (2018) 15, https://doi.org/10.1007/s40820-017-0170-4.

[13] R.K. Hona, F. Ramezanipour, Remarkable oxygen-evolution activity of a perovskite oxide from the $Ca_{2−x}Sr_xFe_2O_{6-\delta}$ series, Angew. Chem. Int. Ed. 58 (2019) 2060–2063, https://doi.org/10.1002/ange.201813000.

[14] J. Saha, S. Verma, R. Ball, C. Subramaniam, R. Murugavel, Compositional control as the key for achieving highly efficient OER electrocatalysis with cobalt phosphates decorated nanocarbon florets, Small 16 (2020), e1903334, https://doi.org/10.1002/smll.201903334.

[15] J. Zhou, Z. Han, X. Wang, H. Gai, Z. Chen, T. Guo, X. Hou, L. Xu, X. Hu, M. Huang, S.V. Levchenko, H. Jiang, Discovery of quantitative electronic structure-OER activity relationship in metal-organic framework electrocatalysts using an integrated theoretical-experimental approach, Adv. Funct. Mater. 31 (2021) 2102066, https://doi.org/10.1002/adfm.202102066.

[16] Z. Sun, L. Lin, J. He, D. Ding, T. Wang, J. Li, M. Li, Y. Liu, Y. Li, M. Yuan, B. Huang, H. Li, G. Sun, Regulating the spin state of Fe^{III} enhances the magnetic effect of the molecular catalysis mechanism, J. Am. Chem. Soc. 144 (2022) 8204–8213, https://doi.org/10.1021/jacs.2c01153.

[17] J. Ge, R.R. Chen, X. Ren, J. Liu, S.J.H. Ong, Z.J. Xu, Ferromagnetic-antiferromagnetic coupling core-shell nanoparticles with spin conservation for water oxidation, Adv. Mater. 33 (2021), e2101091, https://doi.org/10.1002/adma.202101091.

[18] G. Shen, R. Zhang, L. Pan, F. Hou, Y. Zhao, Z. Shen, W. Mi, C. Shi, Q. Wang, X. Zhang, J.J. Zou, Regulating the spin state of Fe^{III} by atomically anchoring on ultrathin titanium dioxide for efficient oxygen evolution electrocatalysis, Angew. Chem. Int. Ed. 59 (2020) 2313–2317, https://doi.org/10.1002/anie.201913080.

[19] S. Zhao, C. Tan, C.-T. He, P. An, F. Xie, S. Jiang, Y. Zhu, K.-H. Wu, B. Zhang, H. Li, J. Zhang, Y. Chen, S. Liu, J. Dong, Z. Tang, Structural transformation of highly active metal-organic framework electrocatalysts during the oxygen evolution reaction, Nat. Energy 5 (2020) 881–890, https://doi.org/10.1038/s41560-020-00709-1.

[20] K. Ge, S. Sun, Y. Zhao, K. Yang, S. Wang, Z. Zhang, J. Cao, Y. Yang, Y. Zhang, M. Pan, L. Zhu, Facile synthesis of two-dimensional iron/cobalt metal-organic framework for efficient oxygen evolution electrocatalysis, Angew. Chem. Int. Ed. 60 (2021) 12097–12102, https://doi.org/10.1002/anie.202102632.

[21] Z. Jiang, X. Xu, Y. Ma, H.S. Cho, D. Ding, C. Wang, J. Wu, P. Oleynikov, M. Jia, J. Cheng, Y. Zhou, O. Terasaki, T. Peng, L. Zan, H. Deng, Filling metal-organic framework mesopores with TiO_2 for CO_2 photoreduction, Nature 586 (2020) 549–554, https://doi.org/10.1038/s41586-020-2738-2.

[22] T.V.M. Sreekanth, G.R. Dillip, P.C. Nagajyothi, K. Yoo, J. Kim, Integration of marigold 3D flower-like Ni-MOF self-assembled on MWCNTs via microwave irradiation for high-performance electrocatalytic alcohol oxidation and oxygen evolution reactions, Appl. Catal. B 285 (2021), 119793, https://doi.org/10.1016/j.apcatb.2020.119793.

[23] W.-D. Zhang, Q.-T. Hu, L.-L. Wang, J. Gao, H.-Y. Zhu, X. Yan, Z.-G. Gu, In-situ generated Ni-MOF/LDH heterostructures with abundant phase interfaces for enhanced oxygen evolution reaction, Appl. Catal. B 286 (2021), 119906, https://doi.org/10.1016/j.apcatb.2021.119906.

[24] G. Kresse, D. Joubert, From ultrasoft pseudopotentials to the projector augmented-wave method, Phys. Rev. B 59 (1999) 1758–1775, https://doi.org/10.1103/PhysRevB.59.1758.

[25] J.P. Perdew, K. Burke, M. Ernzerhof, Generalized gradient approximation made simple, Phys. Rev. Lett. 77 (1996) 3865–3868, https://doi.org/10.1103/PhysRevLett.77.3865.

[26] J.P. Perdew, J.A. Chevary, S.H. Vosko, K.A. Jackson, M.R. Pederson, D.J. Singh, C. Fiolhais, Atoms, molecules, solids, and surfaces: Applications of the generalized gradient approximation for exchange and correlation, Phys. Rev. B 46 (1992) 6671–6687, https://doi.org/10.1103/PhysRevB.46.6671.

[27] J. Tao, J.P. Perdew, V.N. Staroverov, G.E. Scuseria, Climbing the density functional ladder: nonempirical meta-generalized gradient approximation designed for molecules and solids, Phys. Rev. Lett. 91 (2003), 146401, https://doi.org/10.1103/PhysRevLett.91.146401.

[28] M. Yuan, R. Wang, W. Fu, L. Lin, Z. Sun, X. Long, S. Zhang, C. Nan, G. Sun, H. Li, S. Ma, Ultrathin two-dimensional metal organic framework nanosheets with the inherent open active sites as electrocatalysts in aprotic $Li-O_2$ batteries, ACS Appl. Mater. Interfaces 11 (2019) 11403–11413, https://doi.org/10.1021/acsami.8b21808.

[29] R. Turansky, K. Palotas, J. Brndiar, Y.J. Li, Y. Sugawara, I. Stich, Subatomic-scale resolution with SPM: Co adatom on $p(2×1)Cu(110)$:O, Nanotechnology 30 (2019), 095703, https://doi.org/10.1088/1361-6528/aaf6dc.

[30] A.G. Krasnov, M.S. Koroleva, M.I. Vlasov, I.R. Shein, I.V. Piir, D.G. Kellerman, Ab initio and experimental insights into structural, electronic, optical, and magnetic properties of Cr-doped $Bi_2Ti_2O_7$, Inorg. Chem. 58 (2019) 9904–9915, https://doi.org/10.1021/acs.inorgchem.9b01057.

[31] C. Combelles, M. Ben Yahia, L. Pedesseau, M.L. Doublet, Fe^{II}/Fe^{III} mixed-valence state induced by Li-insertion into the metal-organic-framework Mil53(Fe): A DFT+

[32] G. Kresse, J. Furthmüller, Efficiency of ab-initio total energy calculations for metals and semiconductors using a plane-wave basis set, Comput. Mater. Sci. 6 (1996) 15–50, https://doi.org/10.1016/0927-0256(96)00008-0.

[33] Y. Dou, R. Liang, Y. Zhang, Y. Zhao, G. Chen, Y. Wei, Z. Peng, Co_9S_8@carbon porous nanocages derived from a metal-organic framework: a highly efficient bifunctional catalyst for aprotic $Li-O_2$, Batter., J. Mater. Chem. A 6 (2018) 8595–8603, https://doi.org/10.1039/C8TA01913D.

[34] G. Hai, X. Jia, K. Zhang, X. Liu, Z. Wu, G. Wang, High-performance oxygen evolution catalyst using two-dimensional ultrathin metal-organic frameworks nanosheets, Nano Energy 44 (2018) 345–352, https://doi.org/10.1016/j.nanoen.2017.11.071.

[35] S. Zhao, Y. Wang, J. Dong, C.-T. He, H. Yin, P. An, K. Zhao, X. Zhang, C. Gao, L. Zhang, J. Lv, J. Wang, J. Zhang, A.M. Khattak, N.A. Khan, Z. Wei, J. Zhang, S. Liu, H. Zhao, Z. Tang, Ultrathin metal-organic framework nanosheets for electrocatalytic oxygen evolution, Nat. Energy 1 (2016) 16184, https://doi.org/10.1038/nenergy.2016.184.

[36] Y. Peng, Y. Li, Y. Ban, H. Jin, W. Jiao, X. Liu, W. Yang, Metal-organic framework nanosheets as building blocks for molecular sieving membranes, Science (https://www.science.org/doi/) 346 (2014) 1356–1359, https://doi.org/10.1126/science.1254227.

[37] J. Li, X.-H. Zhang, S.-H. You, Q.-X. Wu, S.-M. Chen, K.-N. Zhou, Cr(VI) removal and detoxification in constructed wetlands planted with Leersia hexandra Swartz, Ecol. Eng. 71 (2014) 36–40, https://doi.org/10.1016/j.ecoleng.2014.07.047.

[38] D.M. Morales, M.A. Kazakova, S. Dieckhoefer, A.G. Selyutin, G.V. Golubtsov, W. Schuhmann, J. Masa, Trimetallic Mn-Fe-Ni oxide nanoparticles supported on multi-walled carbon nanotubes as high-performance bifunctional ORR/OER electrocatalyst in alkaline media, Adv. Funct. Mater. 30 (2020) 1905992, https://doi.org/10.1002/adfm.201905992.

[39] X.Y. Li, Z.F. Yao, L.Y. Zhang, G.H. Zheng, Z.X. Dai, K.Y. Chen, Generation of oxygen vacancies on Sr_2FeMoO_6 to improve its photocatalytic performance through a novel preparation method involving pH adjustment and use of surfactant, Appl. Surf. Sci. 480 (2019) 262–275, https://doi.org/10.1016/j.apsusc.2019.02.115.

[40] F. Long, J. He, M. Zhang, X. Wu, S. Mo, Z. Zou, Y. Zhou, Microwave-hydrothermal synthesis of Co-doped FeS_2 as a visible-light photocatalyst, J. Mater. Sci. 50 (2015) 1848–1854, https://doi.org/10.1007/s10853-014-8747-5.

[41] C. Chen, T. Wu, D. Yang, P. Zhang, H. Liu, Y. Yang, G. Yang, B. Han, Catalysis of photooxidation reactions through transformation between Cu^{2+} and Cu^+ in TiO_2-Cu-MOF composites, ChemComm 54 (2018) 5984–5987, https://doi.org/10.1039/C8CC03505A.

[42] C. An, Y. Wang, Y. Wang, G. Liu, L. Li, F. Qiu, Y. Xu, L. Jiao, H. Yuan, Facile synthesis and superior supercapacitor performances of Ni_2P/rGO nanoparticles, RSC Adv. 3 (2013) 4628–4633, https://doi.org/10.1039/C3RA00079F.

[43] T. Wang, X. Guo, J. Zhang, W. Xiao, P. Xi, S. Peng, D. Gao, Electronic structure modulation of NiS_2 by transition metal doping for accelerating the hydrogen evolution reaction, J. Mater. Chem. A 7 (2019) 4971–4976, https://doi.org/10.1039/C8TA11286J.

[44] F.L. Li, Q. Shao, X. Huang, J.P. Lang, Nanoscale trimetallic metal-organic frameworks enable efficient oxygen evolution electrocatalysis, Angew. Chem. Int. Ed. 57 (2018) 1888–1892, https://doi.org/10.1002/anie.201711376.

[45] K. Rui, G. Zhao, Y. Chen, Y. Lin, Q. Zhou, J. Chen, J. Zhu, W. Sun, W. Huang, S. X. Dou, Hybrid 2D dual-metal-organic frameworks for enhanced water oxidation catalysis, Adv. Funct. Mater. 28 (2018) 1801554, https://doi.org/10.1002/adfm.201801554.

[46] D. Voiry, M. Chhowalla, Y. Gogotsi, N.A. Kotov, Y. Li, R.M. Penner, R.E. Schaak, P. S. Weiss, Best practices for reporting electrocatalytic performance of nanomaterials, ACS Nano 12 (2018) 9635–9638, https://doi.org/10.1021/acsnano.8b07700.

[47] C.H. Ahn, W.S. Yang, J.J. Kim, G.S. Priyanga, T. Thomas, N.G. Deshpande, H. S. Lee, H.K. Cho, Design of hydrangea-type Co/Mo bimetal MOFs and MOF-derived Co/Mo_2C embedded carbon composites for highly efficient oxygen evolution reaction, Chem. Eng. J. 435 (2022) 134815, https://doi.org/10.1016/j.cej.2022.134815.

[48] C.-W. Hu, Y. Yamada, K. Yoshimura, Fabrication of nickel oxyhydroxide/palladium (NiOOH/Pd) nanocomposite for gasochromic application, Sol. Energy Mater. Sol. Cells 177 (2018) 120–127, https://doi.org/10.1016/j.solmat.2017.01.021.

[49] H. Li, W. Hao, J. Hu, H. Wu, A photoelectrochemical sensor based on nickel hydroxyl-oxide modified n-silicon electrode for hydrogen peroxide detection in an alkaline solution, Biosens. Bioelectron. 47 (2013) 225–230, https://doi.org/10.1016/j.bios.2013.03.028.

[50] K. Shah, R. Dai, M. Mateen, Z. Hassan, Z. Zhuang, C. Liu, M. Israr, W.C. Cheong, B. Hu, R. Tu, C. Zhang, X. Chen, Q. Peng, C. Chen, Y. Li, Cobalt single atom incorporated in ruthenium oxide sphere: a robust bifunctional electrocatalyst for HER and OER, Angew. Chem. Int. Ed. 61 (2022), e202114951, https://doi.org/10.1002/ange.202114951.

[51] W. Huang, J. Li, X. Liao, R. Lu, C. Ling, X. Liu, J. Meng, L. Qu, M. Lin, X. Hong, X. Zhou, S. Liu, Y. Zhao, L. Zhou, L. Mai, Ligand modulation of active sites to promote electrocatalytic oxygen evolution, Adv. Mater. 34 (2022), e2200270, https://doi.org/10.1002/adma.202200270.

[52] T. Wang, P. Wang, W. Zang, X. Li, D. Chen, Z. Kou, S. Mu, J. Wang, Nanoframes of $Co_3O_4-Mo_2N$ heterointerfaces enable high-performance bifunctionality toward both electrocatalytic HER and OER, Adv. Funct. Mater. 32 (2022) 2107382, https://doi.org/10.1002/adfm.202107382.

[53] G. Hou, X. Jia, H. Kang, X. Qiao, Y. Liu, Y. Li, X. Wu, W. Qin, CoNi nano-alloys modified yolk-shell structure carbon cage via Saccharomycetes as carbon template

for efficient oxygen evolution reaction, Appl. Catal. B 315 (2022), 121551, https://doi.org/10.1016/j.apcatb.2022.121551.

[54] X. Jia, H. Kang, X. Yang, Y. Li, K. Cui, X. Wu, W. Qin, G. Wu, Amorphous Ni(III)-based sulfides as bifunctional water and urea oxidation anode electrocatalysts for hydrogen generation from urea-containing water, Appl. Catal. B 312 (2022), 121389, https://doi.org/10.1016/j.apcatb.2022.121389.

[55] Y. Du, D. Liu, T. Li, Y. Yan, Y. Liang, S. Yan, Z. Zou, A phase transformation-free redox couple mediated electrocatalytic oxygen evolution reaction, Appl. Catal. B 306 (2022), 121146, https://doi.org/10.1016/j.apcatb.2022.121146.

[56] D.C. Nguyen, T.L. Luyen Doan, S. Prabhakaran, D.T. Tran, D.H. Kim, J.H. Lee, N. H. Kim, Hierarchical Co and Nb dual-doped MoS_2 nanosheets shelled micro-TiO_2 hollow spheres as effective multifunctional electrocatalysts for HER, OER, and ORR, Nano Energy 82 (2021), 105750, https://doi.org/10.1016/j.nanoen.2021.105750.

[57] H. Liu, X. Xu, H. Xu, S. Wang, Z. Niu, Q. Jia, L. Yang, R. Cao, L. Zheng, D. Cao, Dual active site tandem catalysis of metal hydroxyl oxides and single atoms for boosting oxygen evolution reaction, Appl. Catal. B 297 (2021), 120451, https://doi.org/10.1016/j.apcatb.2021.120451.

[58] X.-Z. Fan, Q.-Q. Pang, S.-S. Yi, X. Du, S. Zhang, Z.-Y. Liu, X.-Z. Yue, Intrinsic-structural-modulated carbon cloth as efficient electrocatalyst for water oxidation, Appl. Catal. B 292 (2021), 120152, https://doi.org/10.1016/j.apcatb.2021.120152.

[59] L. Yang, H. Ren, Q. Liang, K.N. Dinh, R. Dangol, Q. Yan, Ultrathin amorphous nickel doped cobalt phosphates with highly ordered mesoporous structures as efficient electrocatalyst for oxygen evolution reaction, Small 16 (2020), e1906766, https://doi.org/10.1002/smll.201906766.

[60] Q. Wang, X. Huang, Z.L. Zhao, M. Wang, B. Xiang, J. Li, Z. Feng, H. Xu, M. Gu, Ultrahigh-loading of Ir single atoms on NiO matrix to dramatically enhance oxygen evolution reaction, J. Am. Chem. Soc. 142 (2020) 7425–7433, https://doi.org/10.1021/jacs.9b12642.

[61] T. Ouyang, X.T. Wang, X.Q. Mai, A.N. Chen, Z.Y. Tang, Z.Q. Liu, Coupling magnetic single-crystal $Co_2Mo_3O_8$ with ultrathin nitrogen-rich carbon layer for oxygen evolution reaction, Angew. Chem. Int. Ed. 59 (2020) 11948–11957, https://doi.org/10.1002/anie.202004533.

[62] F. Cheng, Z. Li, L. Wang, B. Yang, J. Lu, L. Lei, T. Ma, Y. Hou, In situ identification of the electrocatalytic water oxidation behavior of a nickel-based metal-organic framework nanoarray, Mater. Horiz. 8 (2021) 556–564, https://doi.org/10.1039/D0MH01757D.

[63] X. Liu, K. Ni, B. Wen, R. Guo, C. Niu, J. Meng, Q. Li, P. Wu, Y. Zhu, X. Wu, L. Mai, Deep reconstruction of nickel-based precatalysts for water oxidation catalysis, ACS Energy Lett. 4 (2019) 2585–2592, https://doi.org/10.1021/acsenergylett.9b01922.

[64] Q. Hu, Y. Xue, J. Kang, I. Scivetti, G. Teobaldi, A. Selloni, L. Guo, L.-M. Liu, Structure and oxygen evolution activity of β-NiOOH: where are the protons? ACS Catal. 12 (2022) 295–304, https://doi.org/10.1021/acscatal.1c04647.

[65] Y. Dou, C.-T. He, L. Zhang, M. Al-Mamun, H. Guo, W. Zhang, Q. Xia, J. Xu, L. Jiang, Y. Wang, P. Liu, X.-M. Chen, H. Yin, H. Zhao, How cobalt and iron doping determine the oxygen evolution electrocatalytic activity of NiOOH, Cell Rep. Phys. Sci. 1 (2020), 100077, https://doi.org/10.1016/j.xcrp.2020.100077.

[66] J. Suntivich, K.J. May, H.A. Gasteiger, J.B. Goodenough, Y. Shao-Horn, A perovskite oxide optimized for oxygen evolution catalysis from molecular orbital principles, Science 334 (2011) 1383–1385, https://doi.org/10.1126/science.1212858.